Corrosion of ferritic–martensitic steels in steam and supercritical water

Jeremy Bischoff [a,b], Arthur T. Motta [a,*], Chad Eichfeld [c], Robert J. Comstock [d], Guoping Cao [e], Todd R. Allen [e]

[a] Department of Mechanical and Nuclear Engineering, Pennsylvania State University, 227 Reber Building, University Park, PA 16802, USA
[b] Areva NP, Fuel Design Materials and Thermal-Mechanics Department, 10 rue Juliette Recamier, 69006 Lyon, France
[c] The Pennsylvania State University Materials Research Institute, NNIN at Penn State, 230 Innovation Boulevard, University Park, PA 16802, USA
[d] Center for Materials Excellence, Westinghouse Electric Co., Pittsburgh, PA, USA
[e] Department of Engineering Physics, University of Wisconsin–Madison, 1500 Engineering Drive, Madison, WI 53706, USA

ARTICLE INFO

Article history:
Available online xxxx

ABSTRACT

Corrosion tests were performed in steam and supercritical water at 500 °C for two ferritic–martensitic alloys: HCM12A and NF616. The corrosion kinetics for the two alloys are similar in both environments showing near cubic behavior, but the corrosion rate was significantly higher in supercritical water than in steam. Examinations of the oxide layers using scanning electron microscopy and microbeam synchrotron diffraction and fluorescence show that both alloys form two-layer oxide structures in either environment. The outer layer contains only Fe_3O_4, while the inner layer contains a mixture of Fe_3O_4 and $FeCr_2O_4$. Additionally, marker experiments using a novel photolithographic deposition process show that the original water–metal interface corresponds with the outer–inner layer interface as expected. The results are discussed in light of known corrosion mechanisms.

© 2012 Elsevier B.V. All rights reserved.

1. Introduction

The Supercritical Water Reactor is one of six Generation IV nuclear power plant designs and was envisioned for its high thermal efficiency and simplified core [1]. This reactor is designed to function at high outlet temperature (between 500 and 600 °C), which requires cladding and structural materials that can perform at these elevated temperatures for extended exposures. Because of their resistance to radiation degradation and stress corrosion cracking, ferritic–martensitic steels such as HCM12A and NF616, are two of the candidate materials, for this reactor, but their resistance to uniform corrosion has to be assessed [2].

In this study both HCM12A and NF616 alloys were exposed in supercritical water (SCW) and in steam, both at 500 °C. The literature shows that these alloys exhibit a three-layer oxide structure when exposed to SCW with an outer layer containing only Fe_3O_4, an inner layer containing a $(Fe,Cr)_3O_4$ spinel structure and a diffusion layer containing a mixture of oxide precipitates primarily on laths boundaries and metal grains [2–13]. Steam corrosion was undertaken to obtain a more detailed understanding of the kinetic behavior of the alloys and revealed a dual-layer structure with Fe_3O_4 in the outer layer and $(Fe,Cr)_3O_4$ spinel in the inner layer as in SCW corrosion [14]. Therefore we could expect the corrosion behavior and kinetics to be similar in both steam and SCW environments as was found to be the case for zirconium alloys [15].

Additionally, micrometric markers were deposited on several samples prior to exposure to steam in order to determine the evolution of the original water–metal interface during corrosion. Although the smoothness of this interface and the absence of Cr in the outer layer suggests that the outer oxide-inner oxide interface is coincident with the initial sample surface no marker experiments had yet confirmed this for these alloys in the SCW environment. Marker studies have been done in the past to study the oxidation behavior of certain steels [16,17] but most of these studies were done using platinum or tungsten wires whose diameter was comparable to the size of the oxide layers formed on ferritic–martensitic alloys (25–70 μm). Such large markers make it difficult to draw clear conclusions because of likely interference with the corrosion process, for example by acting as a barrier for the ion transport. Some experiments have used fine gold powders on pure iron and low chromium ferritic steels [18]. In this study we used a photolithographic technique as the one used by Kim for nickel-based alloys [19].

In this article we characterize the structure of some of these oxide layers using microbeam synchrotron radiation diffraction and fluorescence and electron microscopy. We compare the structure of the oxides formed in steam and in SCW and discuss the influence of the corrosion environment on the differences observed.

2. Experimental procedures

2.1. Alloys studied

The alloys used for this study were NF616 and HCM12A, which are modern ferritic–martensitic alloys. Table 1 shows the elemental composition of these two alloys as given to us by the University

* corresponding author. Tel.: +18148650036.
E-mail address: atm2@psu.edu (A.T. Motta).

Table 1
Chemical composition of the alloys (wt.%).

Alloy	C	N	Al	Si	P	S	Ti	V	Cr	Mn	Fe	Ni	Cu	Nb	Mo	W	Others (ppm)
HCM12A	.11	.063	.001	.27	.016	.002	–	.19	10.83	.64	Bal.	.39	1.02	.054	.3	1.89	B: 31
NF616	.109	–	.005	.102	.012	.003		.194	8.82	.45	Bal.	.174	–	.064	.468	1.87	O: 42

of Wisconsin who supplied us with the material. HCM12A was normalized at 1050 °C for 1 h, air-cooled, then tempered for 7 h at 770 °C and air-cooled. NF616 was normalized at 1070 °C for 2 h, air-cooled, then tempered at 770 °C for 2 h and air-cooled. This metallurgic process creates alloys containing the martensitic lath structure with all the carbon precipitated as $Cr_{23}C_6$ along the lath and prior austenite grain boundaries [20].

2.2. Marker experiment

Markers were placed on corrosion coupons to study the location of the original water–metal interface and the inter-diffusion of species using a photolithographic method similar to the one used by Kim in nickel-based alloys [19]. All the samples, including the ones without any markers, were flattened and polished up to 0.05 colloidal silica to provide a smooth surface, since the flatness and roughness of the sample modifies the focus and the illumination during exposure, which adversely affects the width of the lines. The marker depositions were performed at the Nanofabrication Laboratory at the Pennsylvania State University.

Before starting the photolithographic process, a mask containing the marker pattern was created. The mask consists of a thin film of chromium deposited on a high-quality square glass plate on which the desired pattern is exposed using a Leica EBPG5 E-beam writer. The pattern used was a 1 mm square pattern containing 1-μm thick parallel lines separated by 10 μm.

Fig. 1 illustrates the multi-step process followed to deposit the markers. The first step is to coat the sample surface with thin positive photoresist films. Two layers of photoresist material were deposited: the first (bottom) layer was PMGI SF11 and the second Megaposit SPR 3012. The same coating process was used for both photoresists: static deposition of the photoresist on the sample, immediately followed by spinning at 4000 rpm for 60 s, to achieve an even thickness. After spinning the SF11 photoresist was baked for 10 min at 190 °C. Then the second deposition was performed: the 3012 photoresist was spun and baked for 1 min at 95 °C. The baking in both cases was done on a hot plate.

The second step in the process is to expose the samples in the GCA 8000 i-line stepper. The mask (or reticle) was loaded into the stepper and the stepper scanned through the sample with a 1 mm step size (since the mask was a 1 mm square) exposing at each step for a certain time (1.6–1.8 s). The juxtaposition of the 1 mm squares on the sample forms continuous lines throughout the sample. Right after exposure the 3012 photoresist was developed by placing the samples in the Microposit MF CD-26 developer (tetramethylammonium hydroxide) for 1 min. The developed 3012 photoresist then serves as a mask for the exposure of the SF11 photoresist, which was exposed to deep-UV light for 12 min and developed in XP101 developer (tetraethylammonium hydroxide) for 2 min. The deep-UV exposure-developer step was repeated twice with a 12-min exposure and one extra time with a 3-min exposure each time followed by 2 min development. This redundancy was done to make sure that all the photoresist was removed from the lines where the markers were deposited.

The third step consists of depositing the metal forming the markers on the samples. This was done using a Kurt Lesker electron beam evaporator. After several failed attempts to use platinum (which exhibited poor adherence to the sample surface), it
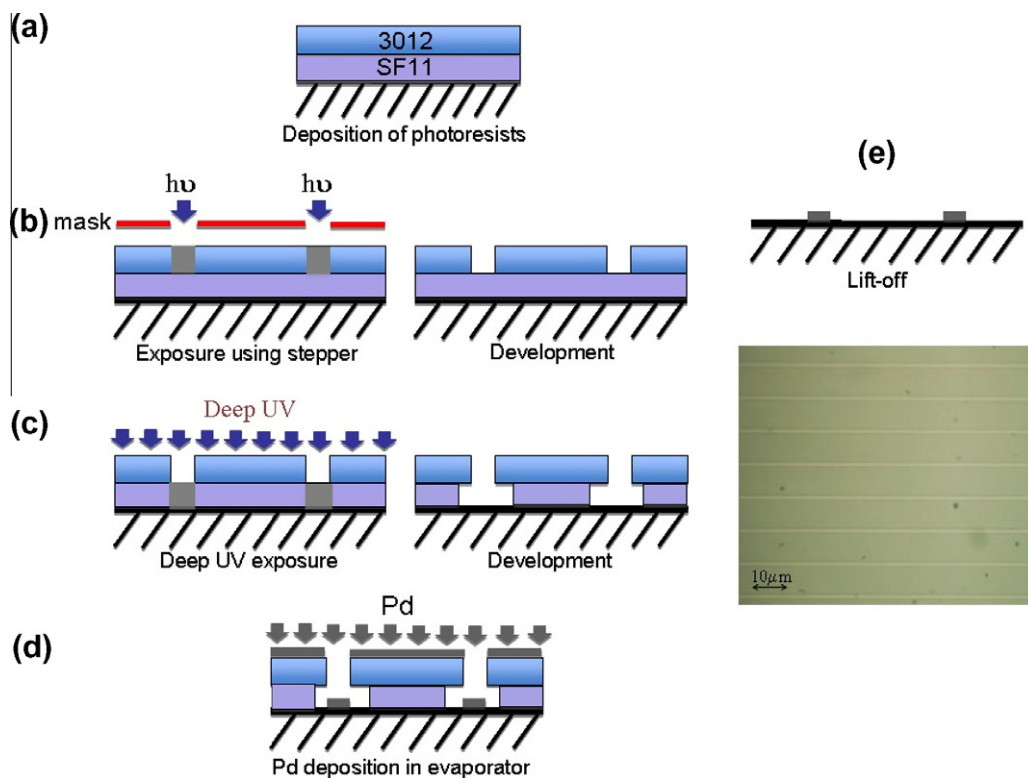
Fig. 1. Photolithographic process to deposit Pd micrometric markers on the sample surface prior to oxidation. The optical image shows the final result on an HCM12A sample.

was decided to use palladium, which has properties similar to platinum. The palladium layer thickness was about 70 nm.

The final step in the process is to remove the remaining photoresist material (lift-off process) to leave only the markers on the sample. The chemical used for the lift-off was the MichroChem Remover PG (N-Methyl Pyrrolidinone). An example of the final results for a marker deposition in HCM12A is shown in the optical image in Fig. 1. This final step removes all the photoresist material from the surface of the sample to obtain a clean sample with a polished surface, as was the case prior to the marker deposition process. If any thin residue subsisted after the lift-off it would get burned off due to the high temperatures of the corrosion experiments so it is safe to assume that no photoresist impeded the oxidation process.

2.3. Corrosion experiments and oxide layer analysis

Corrosion tests were done at 500 °C in both steam and supercritical water. The steam corrosion tests were performed at the Westinghouse Electric Co. in a static deaerated autoclave at a pressure of 10.8 MPa. The SCW tests were performed at the University of Wisconsin in a SCW loop at a pressure of 25 MPa with a dissolved oxygen content of about 10 ppb. The SCW corrosion loop is described in previous articles [21,22]. In both experiments, different coupons were used for each data point to produce the mass gain curves. In each case the mass gain was normalized by the surface of the coupon. All the coupons in both environments had the same surface finish with a polished surface up to a 0.05 μm colloidal silica solution.

The characterization of the oxide layers was performed using scanning electron microscopy (SEM). The SEM images were taken using the backscatter detector of a FEI Quanta 200 ESEM. A few SCW oxide layer samples were analyzed using microbeam synchrotron radiation diffraction and fluorescence. The synchrotron experiment and its experimental procedure have been described in previous articles [5,23–25]. In short, the synchrotron enables to scan through the oxide layer with a step size of 0.2 μm and acquires simultaneous diffraction and fluorescence data at each step. Thus we can "map" the distribution of phases and elements throughout the oxide layer. This technique can differentiate peaks associated with phases that have very similar structures such as Fe_3O_4 and $FeCr_2O_4$ due to its high resolution. The distinction between these two phases is obtained through a more detailed analysis of the peaks as was done in a previous article [5].

3. Results

3.1. Characterization of the oxide layers

Fig. 2 shows SEM images of the oxide layers formed on HCM12A and NF616 during 6 weeks at 500 °C in both steam and SCW. The oxides have a similar two-layer structure (inner oxide and outer oxide) with an additional diffusion layer between the metal and the inner oxide layer [12,13]. The diffusion layer, which is observed in SEM as a slight difference in contrast compared to the metal, contains a mixture of metal grains and large micrometric oxide precipitates that align preferentially along the lath boundaries [6]. The slight difference in contrast forming the diffusion layer is likely caused by the presence of small nanometric oxide precipitates.

The oxide layers formed on HCM12A differ from those formed on NF616 in that they exhibit a more porous outer layer, a denser inner layer, a thicker diffusion layer, and they are thinner overall. The thickness difference between alloys in steam is much less pronounced than in SCW. The SEM images also show that much

thicker oxide layers were formed in SCW than in steam and that both the outer and inner layers appear more porous for the oxides formed in SCW with most of the porosity located at the inner-diffusion layer interface.

Some NF616 and HCM12A samples exposed in supercritical water and steam were analyzed using microbeam synchrotron radiation diffraction and fluorescence. Fig. 3 shows the fluorescence data for the HCM12A 8-week samples oxidized in both SCW and steam. For both samples, the fluorescence data showed no chromium in the outer layer, a chromium-enriched inner layer, and a decrease of the chromium content to reach the alloy base level in the diffusion layer. The iron and chromium fluorescence of the SCW sample exhibits a sharp increase in the diffusion layer due to a refill of the synchrotron beam during acquisition of the data and so has no physical interpretation. The main difference between the SCW and steam fluorescence data is observed in the diffusion layer: in the steam sample the chromium fluorescence is stable in the diffusion layer with a sharp decrease at the diffusion layer-metal interface, whereas in the SCW sample the chromium fluorescence decreases gradually from the inner layer level to that of the metal.

Fig. 4 shows a contour plot of the diffraction data as a function of the diffracted angle 2-theta and the distance from the outer–inner layer interface for HCM12A after 8 weeks in SCW. The contour plot is a 2D projection of the 3D data showing the intensity of the diffracted peaks as a function of distance and the diffraction angle. The diffraction data shows that the outer layer contains only Fe_3O_4, while the inner layer contains a mixture of Fe_3O_4 and $FeCr_2O_4$ with the $FeCr_2O_4$ mainly present near the inner-diffusion layer [5,6,26]. The diffusion layer contains a mixture of metal grains and chromium rich oxide precipitates. The peaks associated with Fe_3O_4 are very narrow in the outer layer because only Fe_3O_4 is present and this layer is composed of large columnar grains. In the inner layer, on the other hand, the grains are small and equiaxed, which broadens the diffraction peaks.

Fig. 5 shows the contour plot of the diffraction data as a function of the diffracted angle 2-theta and the distance from the outer–inner layer interface for HCM12A after 8 weeks in steam. The steam sample exhibits a similar structure to SCW sample except for the presence of strong peaks associated with Cr_2O_3 located at the diffusion layer-metal interface where we had observed a distinct interface with the fluorescence data. This analysis shows that the steam samples exhibit more Cr_2O_3 in the inner and diffusion layers, as was observed with all the samples studied.

3.2. Marker experiment

Fig. 6 shows SEM images of the oxide layers formed on both HCM12A (a and b) and NF616 (c and d) after exposure for 6 weeks to 500 °C SCW (b and d) and steam (a and c) for 6 weeks. The SCW samples were cut along the length of the markers so the markers appear longer than in steam. Overall no significant difference was observed between marked and unmarked samples, which suggests that there is little influence of the markers on the corrosion process.

In both cases the markers are observed at the outer–inner layer interface as expected. This confirms the suggested mechanism of oxidation of ferritic–martensitic steels with an outward migration of iron forming the outer layer and an inward migration of oxygen to form the inner layer. Fig. 7 shows a schematic of this oxidation mechanism.

3.3. Comparison between oxidation in steam and SCW

Fig. 8 shows the various weight gain measurements from the steam and the two SCW experiments for HCM12A and NF616.
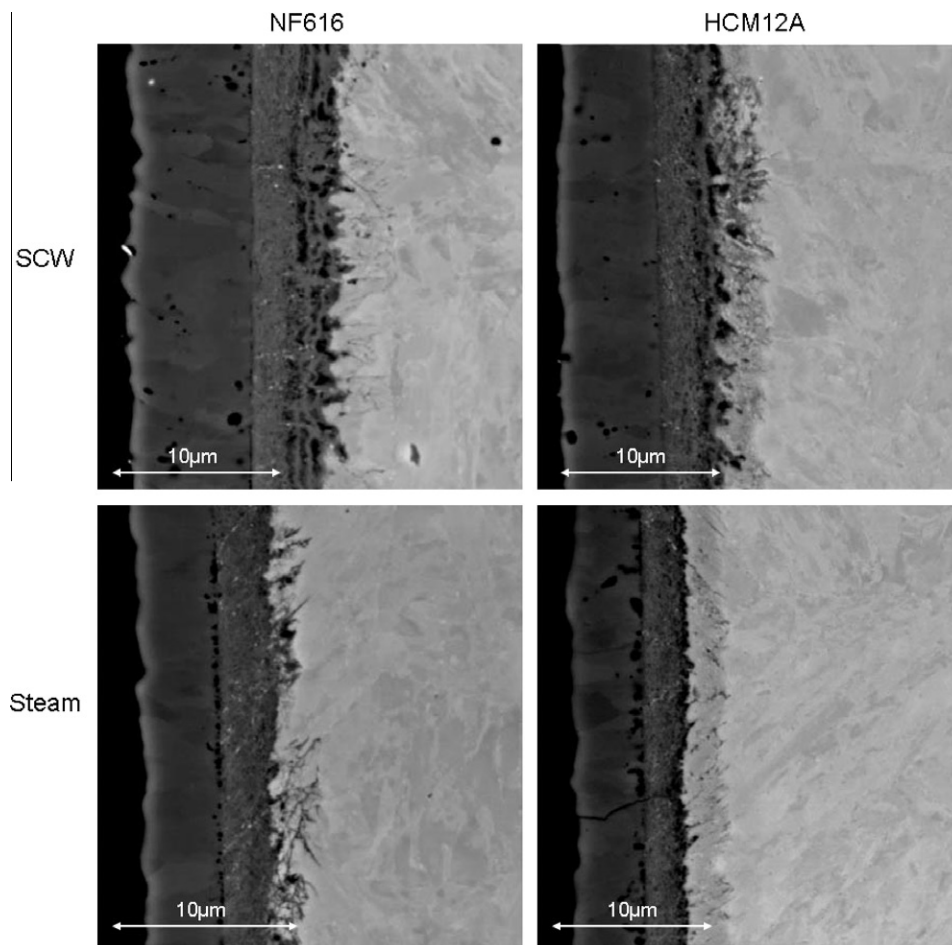
Fig. 2. SEM images of the oxide layers formed on NF616 and HCM12A in both steam and SCW at 500 °C for 4 weeks.

The corrosion rate is commonly expressed by the formula shown in the following equation:

$$W = At^n \qquad (1)$$

with W being the weight gain, A a time constant, t the time and n the corrosion rate exponent.

Table 2 shows the calculated corrosion rate exponents for HCM12A and NF616 in SCW and in steam. The corrosion rates in both environments fall between cubic and parabolic rates, the rates in steam being closer to a cubic rate and slightly lower than the SCW rates. The weight gains for HCM12A and NF616 are similar both in steam and in SCW. The weight gain in steam of NF616 is slightly lower than that of HCM12A, and slightly higher in SCW but it is not clear whether these differences are significant.

For both alloys the weight gain in SCW is 1.5–2 times greater than that in steam, in agreement with the SEM observations in Fig. 2. Thus the corrosion kinetics are not the same in steam and in SCW, contrary to what was observed in the testing of zirconium alloys [15].

4. Discussion

From the data collected, it is difficult to differentiate the effect of the flow in the SCW loop from the difference in corrosion environment. To properly conclude that the environment influences the corrosion kinetics an additional experiment in stagnant SCW should have been performed. Although, such an experiment could not be undertaken in the course of this study, neither could it be done in the case of the study of the zirconium alloys, where no difference in corrosion behavior was observed between the two environments [15]. This suggests that there is an influence of the corrosion environment on the oxidation mechanism, which we discuss in this section.

The results presented in Section 3 show that the SCW samples corroded about 1.5 times faster than the steam samples suggesting a variation in the corrosion behavior caused by the corroding environment. Although the oxides formed in both environments exhibited the same three-layer structure, slight differences in the oxide morphology and microstructure were observed. These differences can help understand the divergence in behavior, and the corrosion mechanism. Overall, in comparison with the oxide formed in SCW, the layers formed in steam were denser, and contained more diffraction peaks associated with Cr_2O_3, especially at the inner-diffusion layer and diffusion layer-metal interfaces where these peaks were intense.

For zirconium alloys, no variation in oxidation behavior was observed between samples corroded in steam and SCW [15]. The fact that such a difference is seen in the alloys studied in this project suggests that the rate-limiting step is different in the two cases. In zirconium alloy corrosion a monolayer of ZrO_2 is formed solely by inward migration of oxygen, with the diffusion of corrosion species through the dense layer being the rate-limiting step. The formation of a multi-layer oxide in ferritic–martensitic alloys is more complex: the outward migration of iron forms the outer layer and the inward migration of oxygen forms the inner layer. The
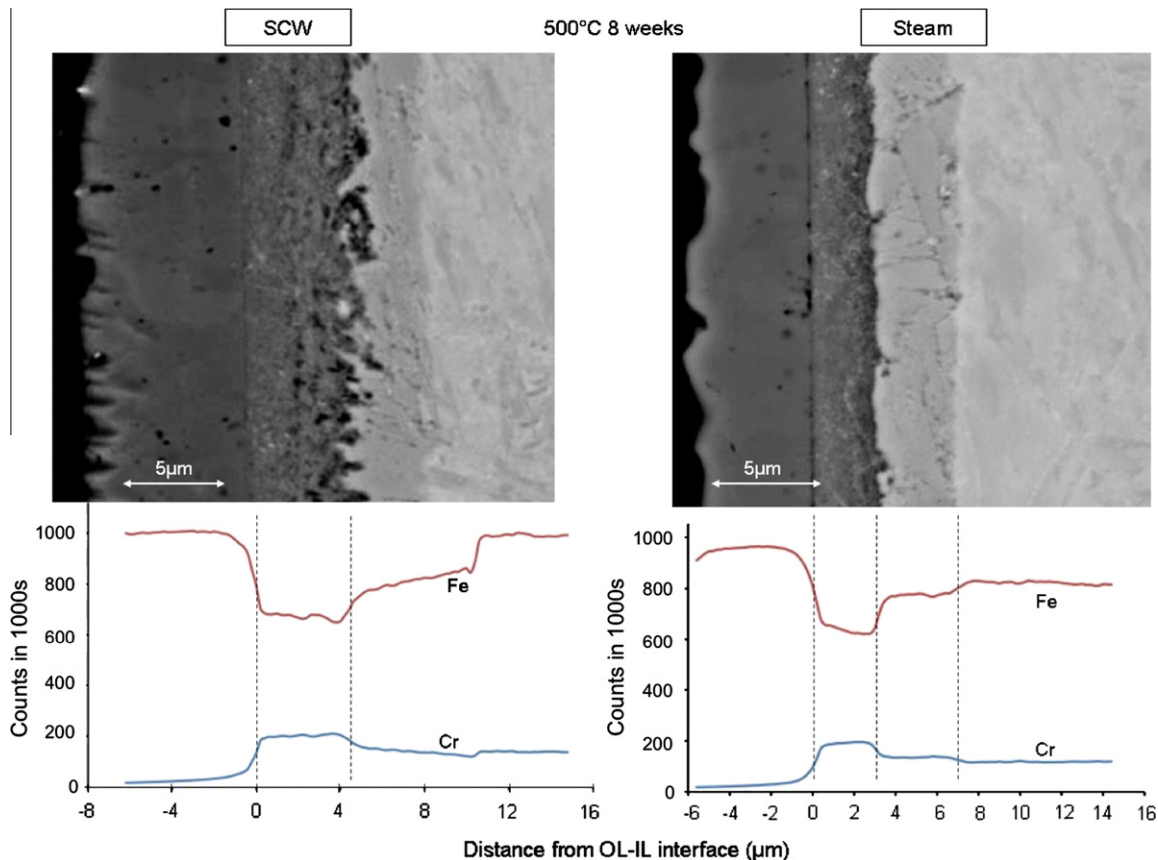
Fig. 3. Fluorescence data for HCM12A samples exposed for 8 weeks in both SCW and steam.
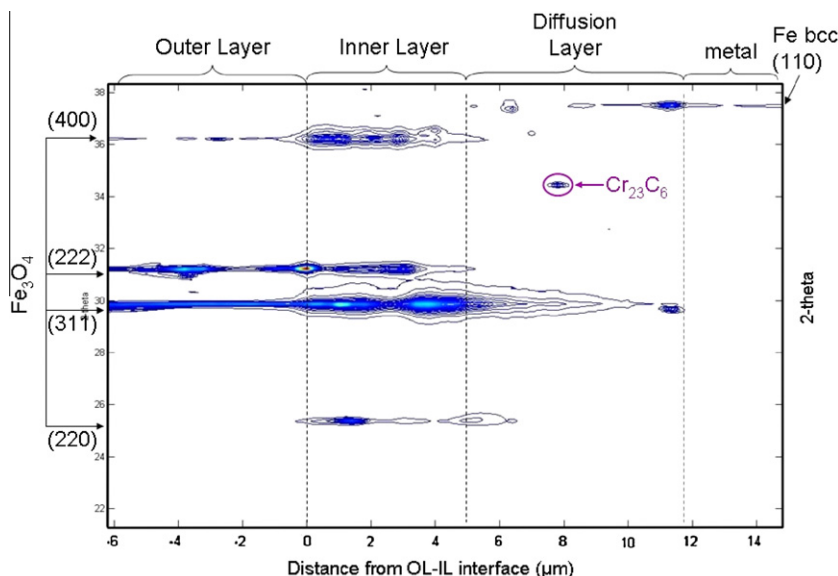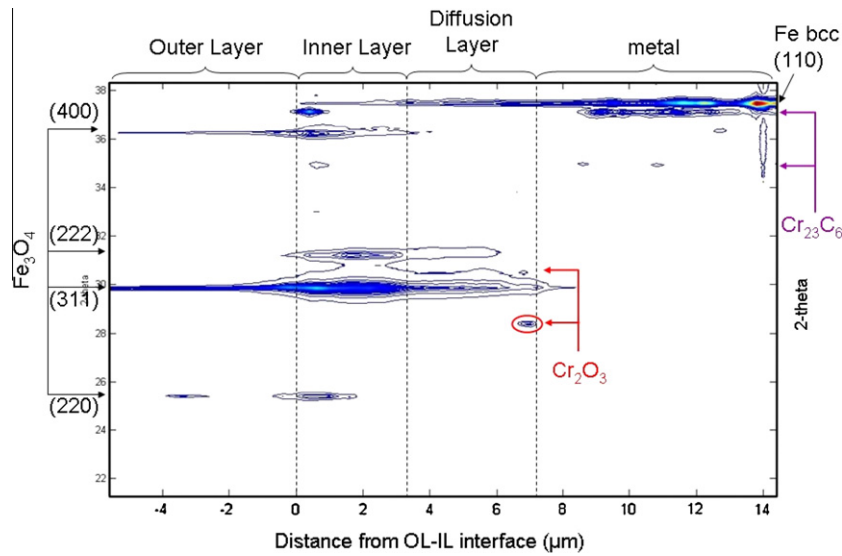

Fig. 4. Contour plot of the diffraction data as a function of the diffracted angle 2-theta and the distance from the outer–inner layer interface for HCM12A exposed to SCW loop for 8.

different oxidation behavior observed between zirconium and ferritic–martensitic alloys suggests that the outward iron migration is the rate-limiting step, as was found in literature [2,11,27–29]. Such a conclusion is consistent with the presence of a diffusion layer in the samples since if oxygen diffusion were the rate-limiting step a diffusion layer would be unlikely to form because the oxygen would not diffuse ahead of the oxide.

In this context, it is interesting to discuss how the difference in corrosion medium affects the outward migration of iron. The dissolved oxygen content during corrosion in steam is low and similar to that in SCW. At such low contents, the dissolved oxygen content has a limited influence on the corrosion kinetics [30]. Since the temperature was identical in both environments, only the pressure increases (10.8 MPa in steam and 25 MPa in SCW), which creates

Fig. 5. Contour plot of the diffraction data as a function of the diffracted angle 2-theta and the distance from the outer–inner layer interface for HCM12A exposed to steam for 8 weeks.
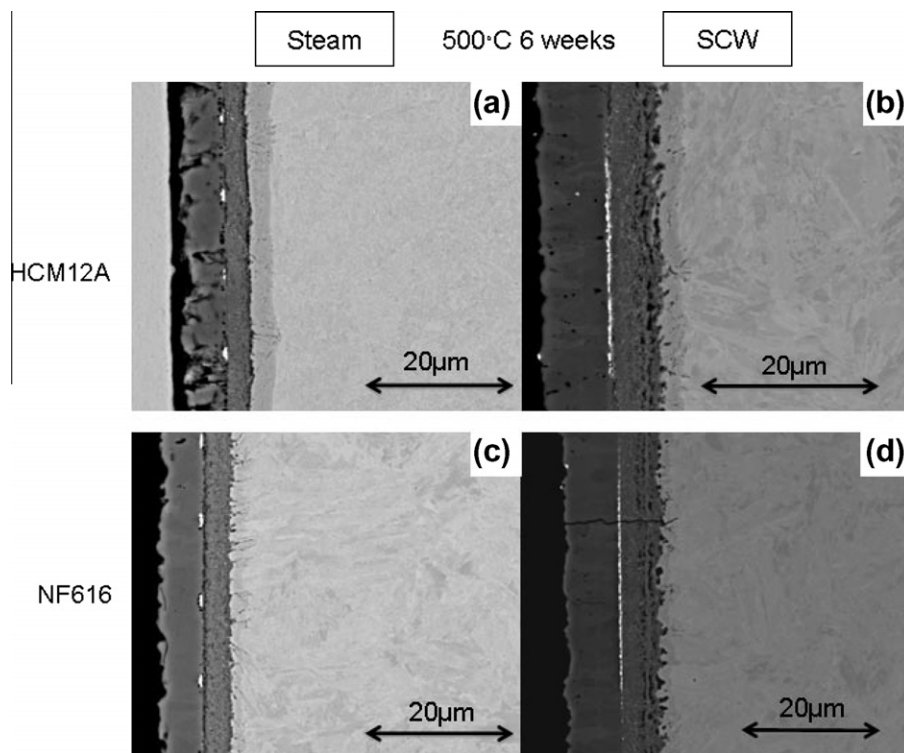
Fig. 6. SEM images of the marked oxide layers formed on HCM12A (a and b) and NF616 (c and d) in 500 °C for 6 weeks in both steam (a and c) and SCW (b and d).
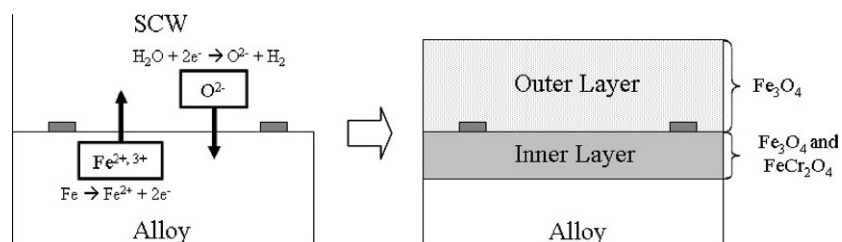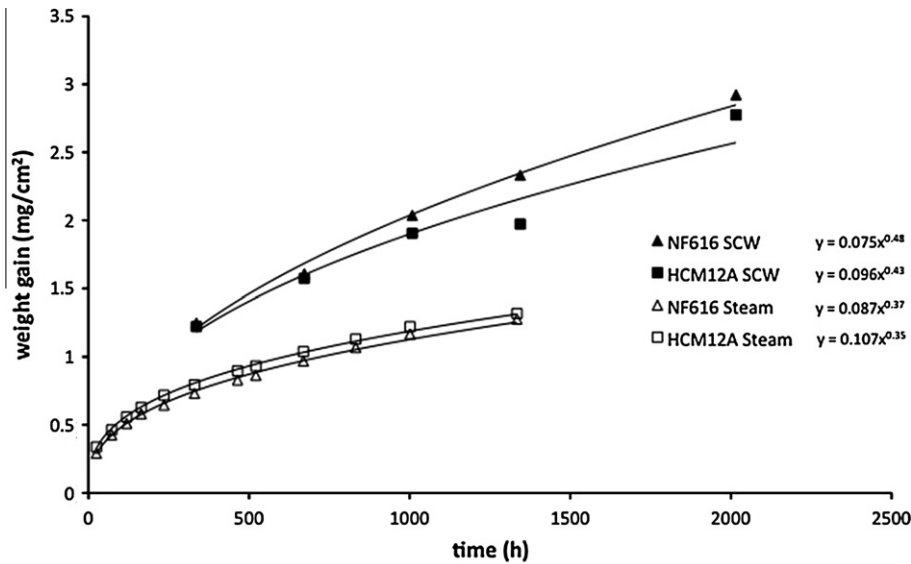

Fig. 7. Schematic of the oxidation mechanism.

Fig. 8. Weight gain measurements from the steam and SCW tests at 500 °C for HCM12A and NF616.

Table 2
Corrosion rate exponents for both alloys in the three corrosion experiments.

Oxidation environment	NF616	HCM12A
Steam	0.37	0.35
SCW	0.48	0.43

larger oxide thicknesses containing additional porosity [14]. The higher pressure in SCW creates a higher density corrosion medium, which can affect corrosion kinetics in two principal ways: by enhancing dissolution of iron ions in SCW thus accelerating the corrosion, or by increasing the number of oxidizing agents adsorbed on the oxide surface [31]. The dissolution of ions into steam and low density SCW remains negligible [31] and therefore it seems more probable that the enhanced corrosion is caused by a larger number of oxidizing agents adsorbed on the sample surface. This has two principal effects: (i) an increase in oxygen content on the outer layer surface, which will enhance the oxidation of

iron from Fe^{2+} to Fe^{3+}, and, (ii) since oxygen diffusion is not rate-limiting, more oxygen can diffuse through the oxide thus increasing the oxygen potential throughout the layers. The oxidation of Fe^{2+} into Fe^{3+} will create a steeper decrease in the Fe^{2+}/Fe^{3+} ratio from the inner-diffusion layer interface to the outer layer surface, thus increasing the driving force for the diffusion of Fe^{2+} towards the outer layer. Since iron diffusion is the rate-limiting step, the increase in iron diffusion leads to increased corrosion. Finally, the increase in oxygen potential throughout the layers will lower the amount of Cr_2O_3 formed (since Cr_2O_3 only forms at low oxygen potential) further enhancing corrosion. Fig. 9 schematically shows the difference in Fe^{2+} to Fe^{3+} ratio at the outer layer surface leading to the increased corrosion in SCW.

The pores observed in the SCW samples are located at the inner-diffusion layer interface. These pores are believed to form through the coalescence of iron vacancies that migrate inward from the more highly oxidized outer layer. Only iron ions (therefore oxidized iron) participate in the outward migration of alloy material through the oxide to form the outer layer. The vacancies, created
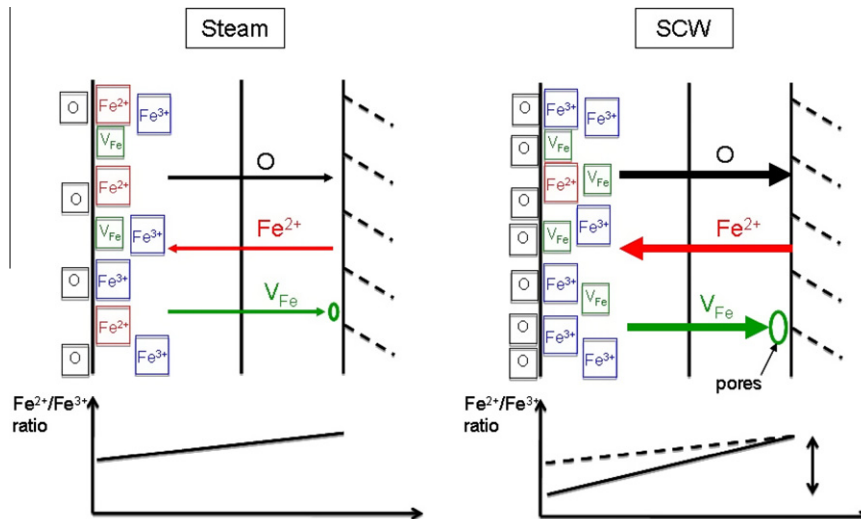

Fig. 9. Schematic of the differences observed between the steam and the SCW corrosion environment leading to differences in oxidation behavior.

to maintain electro-neutrality as the iron is oxidized from Fe^{2+} to Fe^{3+}, then migrate inwards as iron migrates outwards. Since the oxygen potential decreases from the outer to the inner layer, the iron migrates up the oxygen potential while the vacancies migrate down it. Consequently, the regions with the lowest oxygen potential tend to be depleted in iron (and thus enriched in chromium) and exhibit larger porosity. The iron flux through the oxide layer is increased in SCW compared to steam due to a steeper Fe^{2+}/Fe^{3+} ratio gradient so that more vacancies diffuse to the inner-diffusion layer where they coalesce into large pores. This explains the higher porosity observed in the SCW samples compared to the steam samples.

5. Conclusion

Corrosion tests were performed in steam and SCW at 500 °C for two ferritic–martensitic alloys: HCM12A and NF616. A marker experiment was undertaken to determine the location of the original water–metal interface. The oxide structure of the samples was analyzed using microbeam synchrotron radiation diffraction and fluorescence and SEM.

The main conclusions are:

1. Both alloys in both corrosion environments formed a three-layer structure with an outer layer containing only Fe_3O_4 and an inner layer containing a mixture of Fe_3O_4 and $FeCr_2O_4$. Additionally, a diffusion layer composed of a mixture of oxide precipitates and metal grains was formed in the metal ahead of the oxide.
2. After corrosion the markers were located at the outer–inner layer interface, which means that this interface corresponds to the original water–metal interface. This is consistent with a mechanism of outward migration of iron to form the outer layer and inward migration of oxygen to form the inner layer and the diffusion layer.
3. The oxide layers formed in SCW were considerably thicker than in steam and the weight gain data showed a higher corrosion rate in SCW than in steam.
4. The analysis of the difference in oxidation behavior in steam and SCW helps better understand the oxidation mechanism and leads to the following conclusions:
   a. The rate-limiting step for the overall corrosion process is the outward iron migration to form the outer layer.
   b. Iron migrates as ions up the oxygen potential towards the high oxygen potentials present at the outer surface, the ions being oxidized from Fe^{2+} to Fe^{3+} in the process. This leads to a lower Fe^{2+}/Fe^{3+} ratio at the outer layer surface compared to the oxide-metal interface.

The main result of this project was in correlating the evolving oxide microstructure with the corrosion kinetics. Future work will analyze the steam samples using the microbeam synchrotron diffraction and fluorescence and electron microscopy to compare the oxide microstructure in steam with that of the oxide formed in SCW. This will give additional insight on the corrosion mechanisms in steam and SCW.

References

[1] A Technology Roadmap for Generation IV Nuclear Energy Systems, US-DOE-NERAC, 2002.
[2] L. Tan, M.T. Machut, K. Sridharan, T.R. Allen, J. Nucl. Mater. 371 (2007) 161–170.
[3] P. Ampornrat, G.S. Was, J. Nucl. Mater. 371 (2007) 1–17.
[4] J. Bischoff, A.T. Motta, X. Ren, T.R. Allen, in: Proceedings of the 14th Environmental Degradation of Materials in Nuclear Power Systems, American Nuclear Society, 2009, pp. 1764–1770.
[5] J. Bischoff, A.T. Motta, R.J. Comstock, J. Nucl. Mater. 392 (2009) 272–279.
[6] J. Bischoff, A.T. Motta, L. Tan, T.R. Allen, in: Materials for Future Fusion and Fission Technologies, 1125, 2–4 December 2008, Warrendale, PA, Materials Research Society, USA, 2009, pp. 19–24.
[7] Y. Chen, K. Sridharan, T. Allen, Corros. Sci. 48 (2006) 2843–2854.
[8] Y. Chen, K. Sridharan, T.R. Allen, S. Ukai, J. Nucl. Mater. 359 (2006) 50.
[9] Y. Chen, K. Sridharan, S. Ukai, T.R. Allen, J. Nucl. Mater. 371 (2007) 118–128.
[10] A.D. Siwy, T.E. Clark, A.T. Motta, J. Nucl. Mater. 392 (2009) 280–285.
[11] L. Tan, X. Ren, T.R. Allen, Corros. Sci. 52 (2010) 1520–1528.
[12] L. Tan, Y. Yang, T.R. Allen, Corros. Sci. 48 (2006) 4234–4242.
[13] L. Tan, Y. Yang, T.R. Allen, Corros. Sci. 48 (2006) 3123–3138.
[14] I.G. Wright, R.B. Dooley, Int. Mater. Rev. 55 (2010) 129–167.
[15] A.T. Motta, A. Yilmazbayhan, M. Gomes da Silva, R.J. Comstock, G. Was, J. Busby, E. Gartner, Q. Peng, Y.H. Jeong, J.Y. Park, J. Nucl. Mater. 371 (2007) 61–75.
[16] E.M. Fryt, G.C. Wood, F.H. Stott, D.P. Whittle, Oxid. Met. 23 (1985) 1559–1576.
[17] S. Mrowec, T. Werber, M. Zastawnik, Corros. Sci. 6 (1966) 47–68.
[18] V.B. Trindade, R. Borin, B.Z. Hanjari, S. Yang, U. Krupp, H. Christ Jr., Mater. Res. 8 (2005) 365–369.
[19] C.K. Kim, Oxid. Met. 45 (1996) 133.
[20] R.L. Klueh, D.R. Harries, High Chromium Ferritic and Martensitic Steels for Nuclear Applications, ASTM, West Conshohocken, PA, 2001.
[21] K. Sridharan, S.P. Harrington, A.K. Johnson, J.R. Licht, M.H. Anderson, T.R. Allen, Mater. Des. 28 (2007) 1177–1185.
[22] K. Sridharan, A. Zillmer, J.R. Licht, T.R. Allen, M.H. Anderson, L. Tan, in: Proceedings of ICAPP 04, Pittsburgh, PA. 2004. pp. 537.
[23] A.T. Motta, A.D. Siwy, J.M. Kunkle, J.B. Bischoff, R.J. Comstock, Y. Chen, T.R. Allen, in: 13th International Conference on Environmental Degradation of Materials in Nuclear Power Systems, vol. 3, April 19, 2007–April 23, 2007, Whistler, BC, Canadian Nuclear Society, Canada, pp. 1501-1513.
[24] A. Yilmazbayhan, A.T. Motta, R.J. Comstock, G.P. Sabol, B. Lai, Z. Cai, J. Nucl. Mater. 324 (2004) 6–22.
[25] A. Yilmazbayhan, O. Delaire, A.T. Motta, R.C. Birtcher, J.M. Maser, B. Lai, J. Nucl. Mater. 21 (2003) 221–232.
[26] J. Bischoff, A.T. Motta, Y. Chen, T.R. Allen, in: Corrosion, March 22, 2009–March 26, 2009, National Assoc. of Corrosion Engineers International, Atlanta, GA, United States, 2009.
[27] L. Martinelli, F. Balbaud-Célérier, G. Picard, G. Santarini, Corros. Sci. 50 (2008) 2549–2559.
[28] L. Martinelli, F. Balbaud-Célérier, A. Terlain, S. Bosonnet, G. Picard, G. Santarini, Corros. Sci. 50 (2008) 2537–2548.
[29] L. Martinelli, F. Balbaud-Célérier, A. Terlain, S. Delpech, G. Santarini, J. Favergeon, G. Moulin, M. Tabarant, G. Picard, Corros. Sci. 50 (2008) 2523–2536.
[30] G.S. Was, P. Ampornrat, G. Gupta, S. Teysseyre, E.A. West, T.R. Allen, K. Sridharan, L. Tan, Y. Chen, X. Ren, C. Pister, J. Nucl. Mater. 371 (2007) 176–201.
[31] P. Kritzer, J. Supercritical Fluids 29 (2004) 1–29.